The Astrophysical Journal, 986:185 (15pp), 2025 June 20 https://doi.org/10.3847/1538-4357/add474

Explaining Nonmerger Gamma-Ray Bursts and Broad-lined Supernovae with Close Binary Progenitors with Black Hole Central Engines

Christopher L. Fryer[1], Eric Burns[2], Anna Y. Q. Ho[3], Alessandra Corsi[4], Amy Y. Lien[5], Daniel A. Perley[6], Jada L. Vail[3], and V. Ashley Villar[7,8]
[1] Center for Nonlinear Studies, Los Alamos National Laboratory, Los Alamos, NM 87545, USA; fryer@lanl.gov
[2] Department of Physics & Astronomy, Louisiana State University, Baton Rouge, LA 70803, USA
[3] Department of Astronomy, Cornell University, Ithaca, NY 14853, USA
[4] William H. Miller III Department of Physics & Astronomy, Johns Hopkins University, 3400 N. Charles Street Baltimore, MD 21218, USA
[5] Department of Chemistry, Biochemistry, and Physics, University of Tampa, 401 W. Kennedy Boulevard, Tampa, FL 33606, USA
[6] Astrophysics Research Institute, Liverpool John Moores University, IC 2, Liverpool L3 5RF, UK
[7] Center for Astrophysics | Harvard & Smithsonian, 60 Garden Street, Cambridge, MA 02138-1516, USA
[8] The NSF AI Institute for Artificial Intelligence and Fundamental Interactions, USA
Received 2024 October 14; revised 2025 April 19; accepted 2025 May 3; published 2025 June 17

Abstract

For over 25 yr, the origin of long-duration gamma-ray bursts (lGRBs) has been linked to the collapse of rotating massive stars. However, we have yet to pinpoint the stellar progenitor powering these transients. Moreover, the dominant engine powering the explosions remains open to debate. Observations of both lGRBs, supernovae associated with these GRBs, such as broad-line (BL) stripped-envelope (type Ic) supernovae (hereafter, Ic-BL), supernovae (SNe), and perhaps superluminous SNe, fast blue optical transients, and fast x-ray transients, may provide clues to both engines and progenitors. In this paper, we conduct a detailed study of the tight-binary formation scenario for lGRBs, comparing this scenario to other leading progenitor models. Combining this progenitor scenario with different lGRB engines, we can compare to existing data and make predictions for future observational tests. We find that the combination of the tight-binary progenitor scenario with the black hole accretion disk engine can explain lGRBs, low-luminosity GRBs, ultra-long GRBs, and Ic-BL. We discuss the various progenitor properties required for these different subclasses and note such systems would be future gravitational-wave merger sources. We show that the current literature on other progenitor-engine scenarios cannot explain all of these transient classes with a single origin, motivating additional work. We find that the tight-binary progenitor with a magnetar engine is excluded by existing observations. The observations can be used to constrain the properties of stellar evolution, the nature of the GRB, and the associated SN engines in lGRBs and Ic-BL. We discuss the future observations needed to constrain our understanding of these rare, but powerful, explosions.

Unified Astronomy Thesaurus concepts: Supernovae (1668); Type Ic supernovae (1730); Gamma-ray bursts (629); Massive stars (732)

1. Introduction

Gamma-ray bursts (GRBs) are the most luminous events in the Universe. Although they were discovered over 50 yr ago (R. W. Klebesadel et al. 1973), the true power of these explosions was not fully understood until distance measurements allowed for quantification of their intrinsic brightness (D. A. Frail et al. 1997; M. R. Metzger et al. 1997; J. S. Bloom et al. 1998). While the community quickly converged on a narrow set of possible long-duration gamma-ray burst (lGRB) engine and progenitor models, their exact properties are still not fully understood. With better studies of different progenitors and engines, we can both learn more from observations of these explosions and better understand their role in the menagerie of transient outbursts observed in the Universe.

Proposed GRB engines fall into three major engine paradigms (C. L. Fryer et al. 2019): (a) black hole accretion disk engines (BHAD) powered either by energy in the disk or the rotating black hole (S. E. Woosley 1993; R. Popham et al. 1999), (b) magnetar engines powered by the rotational energy in a spinning neutron star (NS; J. C. Wheeler et al. 2000; B. Zhang & P. Mészáros 2001), or (c) NS accretion disk (NSAD) powered by the energy in a disk around an NS (F. C. Michel 1985). The progenitors of these engines are very similar. Most progenitors are either the mergers of compact objects (e.g., NS mergers with black holes, NSs, or white dwarfs; for the magnetar engine, this includes white dwarf/white dwarf mergers) or the collapse of the cores of massive stars from either massive stars or through the merger of a compact object with a massive star (C. L. Fryer et al. 1999).

C. L. Fryer et al. (2007) summarized a community consensus of the different progenitor scenarios of lGRBs, reviewing many of the relevant observations constraining the GRB progenitor scenario, including the rate, associated supernova (SN), metallicity, surrounding environment, host type, and distribution within the host (offsets). The progenitors considered spanned many of the leading progenitors proposed at the time. These included single stars, both with normal stellar mixing parameters (S. E. Woosley 1993; C. L. Fryer et al. 1999) and with extended mixing, a.k.a., homogeneous stars (S. C. Yoon & N. Langer 2005). A number of binary progenitors were also considered (many from the previous extensive study by C. L. Fryer et al. 1999) including short-period binaries allowing tidal spin-up (E. P. J. van den Heuvel & S. C. Yoon 2007) and a broad set of merger scenarios

(N. Ivanova & P. Podsiadlowski 2003; C. L. Fryer & A. Heger 2005) including mergers with a single compact object (C. L. Fryer & S. E. Woosley 1998). The binary-driven hypernova model (J. A. Rueda & R. Ruffini 2012; C. L. Fryer et al. 2014) required tight binaries to drive the accretion-induced collapse, arguing that the supernova would be from a stripped star (type Ic). A set of cluster formation scenarios were also studied (S. F. Portegies Zwart et al. 2005). For the most part, this study reviewed the different scenarios. None of the progenitors studied by C. L. Fryer et al. (2007) fit the observations perfectly. Because of this, and because there were concerns that the observational interpretations could be wrong, these progenitors persisted.

For example, most progenitor models foresee a GRB jet propagating through a wind circumstellar medium, but a large fraction of lGRB observations seem to be better fit by a constant-density interstellar medium (ISM) profile (R. A. Chevalier & Z.-Y. Li 2000; A. Panaitescu 2005). While expansion in the ISM would argue against massive-star progenitors, the GRBs appeared to occur in star-forming galaxies and star-forming regions (K. M. Svensson et al. 2010). Hence, it was assumed that approximations in the afterglow models may lead to a misinterpretation of the observations as favoring the ISM constant-density profile. As we produce more accurate afterglow models and build better progenitor models (including a better understanding of stellar mass-loss), afterglow observations may provide crucial input to the progenitors (and stellar mass-loss itself).

The currently favored engine and progenitor for lGRBs is the collapsar model (S. E. Woosley 1993) that invokes the collapse of the rotating core of a massive star. Note that throughout this paper we are focusing on lgrbs from collapsars, and neglecting the contribution of lgrbs that arise from mergers (J. C. Rastinejad et al. 2022; A. J. Levan et al. 2024). The classic collapsar model relies on the BHAD engine and a number of potential progenitors to produce the required rotation speeds (for reviews, see C. L. Fryer et al. 1999, 2007). Because GRBs are rare, it is difficult to identify the exact progenitor or progenitors of this engine for long-duration bursts. Less than 1 in 1000 of all stellar collapses produce GRBs (A. Lien et al. 2014; D. A. Perley et al. 2020). This rate is uncertain, depending on both estimates of the total observed rate and the beaming angle (P. Kumar & B. Zhang 2015). Roughly 1 in 10 stellar collapses make black holes (C. L. Fryer & V. Kalogera 2001), so this means that $<1\%$ of all black hole forming systems are needed to explain the bulk of all lGRBs. With such a small fraction of systems producing these explosions, a wide range of, at times exotic, progenitor scenarios are possible. If we include other engine scenarios (e.g., magnetar or NSAD), identifying the exact progenitor proves even more difficult.

One of the key observations that provide insight into the progenitors producing lGRBs is the nature of the SNe often associated with lGRBs (S. Woosley & J. Bloom 2006; Z. Cano et al. 2017). Initially called hypernovae (K. Iwamoto et al. 1998), the broad-line (BL) features from the high-velocity Doppler broadening of these explosions (P. A. Mazzali et al. 2002) led to the adoption of the BL SN nomenclature. Hypernovae or BL SNe refer to any SNe with high-velocity (15,000–20,000 km s^{-1}) features at the peak of the optical light curve, regardless of whether they are associated with GRBs. Thus far, the observed BL SNe are all type Ic, i.e., stripped-envelope with little or no evidence of H or He lines (M. Modjaz et al. 2016). Hence, progenitor models for these Ic-BL SNe require the SN explosion to either prevent any helium emission (e.g., by completely ionizing the helium) or shed the helium before the explosion.

There is growing evidence that Ic-BL SNe, whether or not associated with GRBs, are produced by the same GRB engine/progenitor scenario (e.g., E. Sobacchi et al. 2017; J. Barnes et al. 2018; and M. Modjaz et al. 2020; more on this is Section 7). If we assume that all Ic-BL SNe are produced by the same engine (e.g., BHAD, magnetar) mechanism, we can use the entire population of Ic-BL SNe to probe the nature of the progenitor and engine. Viewing angle effects could explain the diversity of GRB strengths and their relation to Ic-BL SNe (J. Barnes et al. 2018). In this paper, we instead assume that differences in the duration and power of the engine (caused by differences in the progenitor) explain not only the different types of long-duration bursts but also Ic-BL supernovae with and without GRBs.

In this paper, we focus on the tidally spun-up progenitor scenario of lGRBs to determine whether it can explain both the required spins and the lack of helium in the exploding star. Tidal spin-up scenarios after a hydrogen common envelope phase have had mixed results (compare R. G. Izzard et al. 2004; R. G. Detmers et al. 2008) and determining whether tidal spin-up can produce enough fast-rotating systems to explain GRBs remains an open question. Our standard picture is that a second helium common envelop mass ejection is required. But it is also possible that the common envelop phase injects hydrogen in the helium shell, causing a violent explosion that ejects the helium shell (P. Podsiadlowski et al. 2010). One of the difficulties in understanding these progenitors is the range of results arising from stellar codes, and we consider a range of stellar models in our study of angular momenta and compact remnant spins (Section 2). We compare the results from these tidally locked binaries (we include both He- and CO-star binaries) with those of single stars. With these angular momentum results, we then study the predictions of the magnetar model (Section 3) and the BHAD model using a number of mechanisms producing the jet (Section 4). This analysis refines the predictions of our tidally locked binary scenario for the properties of GRBs and SNe (Section 5). These predictions are then compared to SN (particularly Ic-BL) observations in Section 6 and GRB properties in Section 7. In each of these two sections, we both compare predictions to current observations and argue for future observations that will further constrain our engine and progenitor models. We conclude with a review of our results and a comparison to other potential progenitors.

2. Angular Momentum and Compact Remnant Spins

Whether the lGRB engine is a magnetar, an NSAD, or a BHAD, the collapsing star must have considerable angular momentum to produce the powerful jets observed in GRBs. This is difficult to achieve in single star models. The problem arises from the fact that when massive stars expand off the main sequence, angular momentum conservation causes their spin rate to decrease. If the stellar core is coupled to the envelope such that its spin is set to the envelope spin, the collapsed core will not have enough angular momentum to drive a GRB engine. A number of scenarios have been proposed to either retain the high spin rate or spin up the star (C. L. Fryer et al. 1999). A broad range of stellar and compact remnant observations (e.g., pulsars, X-ray binaries, and

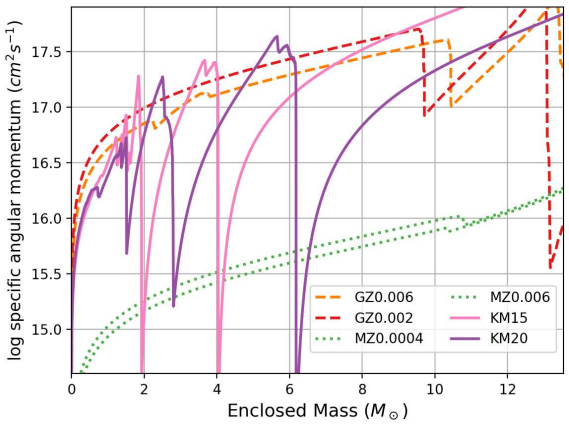

Figure 1. Angular momentum for three different mechanisms coupling the angular momenta between burning layers. The Genec models (GZ0.006, GZ0.002), which use no magnetic coupling between burning layers, correspond to a 32 $M_\odot$ star with metallicities set to 0.006 and 0.002. Metallicity only mildly affects the spin rates for the 32 $M_\odot$ star. The Kepler models (KM15, KM20) use a mild Taylor-Spruit dynamo that reproduces pulsar spin velocities. These models use 15 and 20 $M_\odot$ solar metallicity progenitors. The primary differences in the angular momentum profiles between the Genec and Kepler models lie in this burning layer coupling. The Kepler models are evolved to collapse. The MESA models (M0.006, M0.0004) were run with strong magnetic coupling between burning layers for a 40 $M_\odot$ star. This coupling highlights the strong dependence of the spin on the prescription for magnetic coupling.

merging black hole systems) have been leveraged to provide clues into the nature of the spins in stellar cores (K. Belczynski et al. 2020). These observations suggest a wide range of core spin periods.

The diversity in the rotation periods of current models of massive stars lies principally in the prescription of the coupling of angular momentum between burning layers. Figure 1 shows the specific angular momentum for a range of different models, varying mass, metallicity and, most importantly, the method used to couple the different burning layers. For single star models, the fastest-spinning cores are produced by the GENEC (P. Eggenberger et al. 2008) simulations that do not include strong coupling between burning layers. The KEPLER (A. Heger et al. 2005) models include a Taylor-Spruit dynamo coupling the stellar boundaries, producing slower rotating models. Also shown are MESA (B. Paxton et al. 2013) models using its version of the Taylor-Spruit dynamo with strong coupling from the high-magnetic field MESA models used in the K. Belczynski et al. (2020) paper. The differences in the angular momentum are primarily due to the very different schemes used in these particular calculations to couple the different burning layers for these calculations and not in the codes themselves. One other major difference is that the KEPLER models are modeled to collapse and the GENEC and MESA models are modeled to the onset of silicon burning.

For this paper, we primarily focus on the different angular momentum profiles. Typically, a specific angular momentum above $\sim 10^{17}$ cm^2 s^{-1} is needed within the inner 1.4–2 $M_\odot$ of the stellar core so that the NS spin energy equals 10^{52} erg or a black hole accretion disk whose extent is 3 times that of the innermost stable circular orbit. For black hole accretion disk systems, this can be achieved if the coupling is weak, but it is impossible for stars that are strongly coupled (Genec models—dotted lines). But none of these models work for our magnetar engine. We will discuss the ramifications of these results in Sections 3 and 4.

From the angular momentum of these stars, we can calculate the spin of the NS or BH formed in the collapse by assuming the angular momentum in the star is preserved during the collapse and formation of the compact remnant. However, this simple prescription would overestimate the total angular momentum. If the angular momentum is sufficiently high that the material is centrifugally supported prior to its incorporation into the compact remnant, it will hang up in a disk. This material must lose a fraction of its angular momentum to add its mass to the compact remnant. This places an upper limit on the angular momentum accreted. For NSs, this upper limit ($j^{\rm NS}_{\rm max}$) is:

$$j^{\rm NS}_{\rm max} = \sqrt{GM_{\rm NS} r_{\rm NS}} \quad (1)$$

where G is the gravitational constant, $M_{\rm NS}$ is the compact remnant mass during the accretion, and $r_{\rm NS}$ is the NS radius. To estimate the NS spin, we collapse layer after layer of the star where the mass of the NS is:

$$M^k_{\rm NS} = M^{k-1}_{\rm NS} + dm^k \quad (2)$$

where the k refers to the layer or zone from the stellar model, and dm^k is the mass of that zone. The corresponding angular momentum of this accreting NS is:

$$J^k_{\rm NS} = J^{k-1}_{\rm NS} + \min(j^k, j^{\rm NS}_{\rm max}) dm^k \quad (3)$$

where j^k is the specific angular momentum in zone k. During formation, the NS is hot and more extended than its final radius. To get an upper limit on the angular momentum accreted for BH-forming systems, we assume $j^{\rm NS}_{\rm max}$ is set by this extended radius ($\sim$30 km). For systems that ultimately form an NS, we use a more compact 10 km radius. Figure 2 shows the expected spin periods for a set of massive stars, NS-forming progenitors as well as the spins of NSs in the initial collapse of BH-forming progenitors. The single star models compare the results of the spins conserving the angular momentum profiles before and after silicon burning assuming weak Taylor-Spruit coupling as is used in most Kepler calculations (solid lines). During silicon burning, angular momentum in the iron core is lost to the silicon layer, reducing the final NS spin period. Since many stellar calculations only evolve the star to the onset of silicon burning, many spin estimates will be limited to these models, which could overestimate the spin periods by an order of magnitude.

Our single star models all used rapidly spinning progenitors (at formation, these stars are all within a factor of 2 of breakup spin velocities). For these single stars with Taylor-Spruit coupling, the fastest NS spin periods are all above a few milliseconds. These models are a good fit for the pulsars with the fastest at-birth spins (C. A. Faucher-Giguère & V. M. Kaspi 2006; A. Noutsos et al. 2013). The fastest spins are produced by stars that collapse to form NSs. But, as we shall discuss below, these stars struggle to produce the high energies seen in GRBs. Any observations of a $\sim$1 ms pulsar at birth is either an indication that the angular momentum coupling is not as strong as the Taylor-Spruit dynamo predicts or that tidal spin-up has occurred. It is possible to gain angular momentum in the explosion itself from nonrotating stars. Simulations have produced birth spins anywhere between 10 ms to many seconds from a nonrotating or slowly rotating star (J. M. Blondin & A. Mezzacappa 2007;

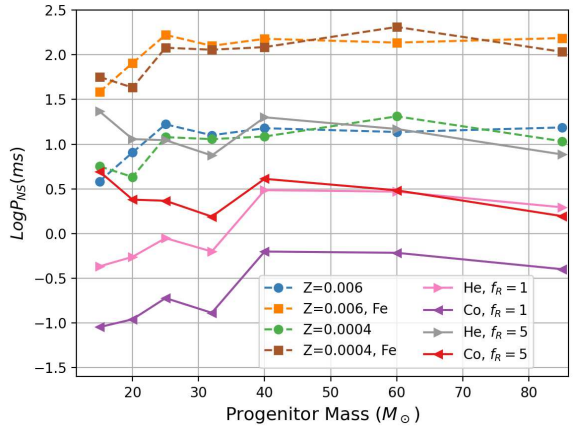

Figure 2. Spin periods of NSs formed in the collapse of massive stars. Those stars where the proto-NS would collapse through continued accretion prior to cooling have spin periods calculated assuming a 30 km proto-NS radius. Progenitors that form NSs assume a final NS radius of 10 km. The $Z = 0.006$, $Z = 0.0004$ models correspond to different metallicities. Models without the "Fe" correspond to spin periods calculated assuming the angular momentum is set by the state prior to silicon burning, and the "Fe" models correspond to stars assuming mild coupling through the collapse of the iron core. The He, CO models correspond to He and CO stars where the orbital separation is set to a factor f_R times the Roche limit of a primary star with a 2 $M_\odot$ compact companion.

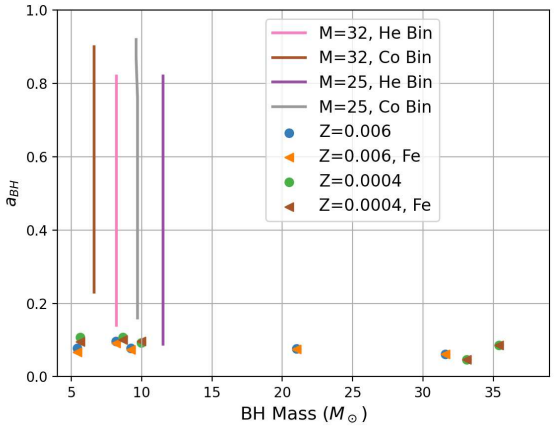

Figure 3. Black hole spins formed from our stellar collapse models. Here we limit the models to black hole forming stars and estimate the mass from the rapid models of C. L. Fryer et al. (2012). The single-star and binary models considered are the same as those in Figure 2 where the lines for the binary models correspond to separations ranging from 1.1–5 times the Roche limit. Here we calculate the Roche limit assuming a 2 $M_\odot$ compact companion.

C. L. Fryer & P. A. Young 2007; E. Rantsiou et al. 2011; A. Wongwathanarat et al. 2013; A. Burrows et al. 2024). As we shall see in Section 3, more rapid spins are required for the magnetar engine to produce lGRBs.

Hereafter, we focus on tight binaries that undergo tidal spin-up. Common envelope mass loss can produce a wide range of helium star binaries with either a main sequence or compact object companion. For this study, we assume the structure of the star is not too dissimilar to that of the structures produced by single star evolution.[9] For these binaries, we follow the approach of K. Belczynski et al. (2020) and assume solid body rotation.[10] Further removing the helium envelope through binary mass transfer will require very tight binaries, most likely with compact companions. In Figure 2, we assume only the tightest binaries, assuming a compact binary with an orbital separation set to a factor, f_R, of the Roche limit. Here we set the Roche limit by assuming a 2 $M_\odot$ compact companion. The separation of the binary is then a factor of f_R times bigger than this closest separation. For these tight, tidally spun-up stars, the spin periods can fall below 1 ms. As we shall discuss in Section 3, such fast spins will lead to instabilities that remove angular momentum from the system.

Conservation of angular momentum can also be used to estimate the mass and spin of the black hole. We set the maximum angular momentum accreted onto the black hole ($j^{\rm BH}_{\rm max}$) to:

$$j^{\rm BH}_{\rm max} = \sqrt{GM_{\rm BH} r_{\rm EH}} \quad (4)$$

where $M_{\rm BH}$ is the black hole mass and where we assume the angular momentum is lost until the matter reaches the event horizon. Studies suggest that angular momentum must be lost within the ISCO (C. Bambi & E. Barausse 2011), but our strict assumption places a lower limit on the angular momentum gained. For the event horizon ($r_{\rm EH}$), we use:

$$r_{\rm EH}/r_{\rm Schwarzschild} = \frac{1 + \sqrt{1 - a^2\cos(\theta)^2}}{2} \quad (5)$$

where, because we are interested in the plane of the angular momentum, $\theta = \pi/2$, and we use

$$r_{\rm Schwarschild} = 2GM_{\rm BH}/c^2 \quad (6)$$

where c is the speed of light. But disk formation can also alter the mass accretion. In disk models, a nonnegligible amount of mass is ejected along with the angular momentum. These disk winds can eject anywhere from 1% to 30% of the disk mass. Ultimately, the energy injected into the star from the GRB jet and the accretion disk wind will prevent further accretion. This process is not well understood and, for our initial black hole mass and spin estimates, we will only include the mass loss from the disk wind. The resulting black hole masses and spins are:

$$M^k_{\rm BH} = M^{k-1}_{\rm BH} + dm^k(1 - f_{\rm wind}) \quad (7)$$

and

$$J^k_{\rm BH} = J^{k-1}_{\rm BH} + \min(j^k, j^{\rm BH}_{\rm max})dm^k. \quad (8)$$

The resulting spins for black holes using our models are in Figure 3.

For single stars using the Spruit-Taylor dynamo, black hole spins tend to be 0.1. Such models are consistent with the observed spins from gravitational-wave binaries (K. Belczynski et al. 2020). But a subset of BHs in these binaries appear to be spinning more rapidly. One explanation for the progenitors of such BHs is that they are spun up through tidal forces in a close binary. The angular momentum profiles for these binaries lie somewhere between the "no coupling" GENEC calculations and the more strongly coupled MESA models (Figure 4). The closer

[9] The loss of the hydrogen layer from common envelope mass ejection shuts off hydrogen shell burning. By itself, this typically alters the helium core by <10%. However, if this common envelope mass ejection initiates strong Wolf–Rayet winds, it can have a more dramatic effect on the core. We defer a more complete study of this to a later paper.

[10] Solid body rotation is a reasonable assumption if massive stars behave similarly to low-mass stars and the inferred constraints on the magnetic coupling are high (J. Fuller et al. 2019; P. Eggenberger et al. 2022). More details on these assumptions can be found in K. Belczynski et al. (2020).

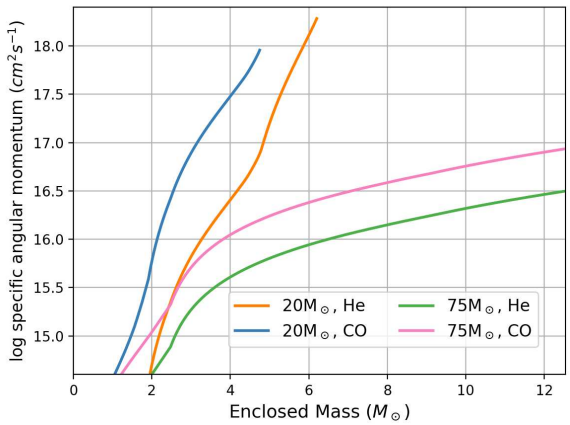

Figure 4. Angular momentum vs. enclosed mass for four tidally locked binaries assuming separations near the Roche limit for CO and He stars with zero-age main-sequence progenitor masses of 20, 75 $M_\odot$. Here, we calculate the Roche limit assuming the companion star is a 2 $M_\odot$ compact companion. The angular momentum for all of these models exceeds 10^{17} cm^2 s^{-1} for all of our models, but the 20 $M_\odot$ produces extremely high angular momenta.

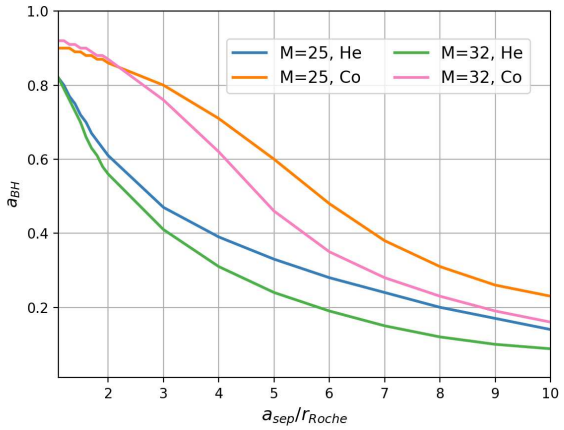

Figure 5. Black hole dimensionless spin parameter vs. of orbital separation (in Roche limits) for four models assuming He and CO stars for 25, 32 $M_\odot$ zero-age main-sequence mass progenitors. Here, we calculate the Roche limit assuming the companion star is a 2 $M_\odot$ compact companion. Spin rates above 0.4 are expected for models that produce reasonable disks.

binaries produced in CO core binaries lead to higher angular momenta at any given mass coordinate, but the helium stars are more extended, and the outermost layers can have specific angular momenta that exceed that of the CO stars.

The angular momentum in these binary systems depends upon how close the binaries become. Figure 4 assumed tight binaries just above the Roche limit where mass transfer would occur. The lines in Figure 3 show the expected spin parameters for orbital separations for these black holes ranging from 1.1–5 Roche limit. The separation of the binary is set by when the common envelope phase ejects the envelope. For He-star-forming binaries, the initial separation can be anywhere where the hydrogen giant phase can envelope the companion. These common envelope systems can form a wide range of separations, leading to systems that form black holes across (and beyond) the range shown in Figure 5. But helium common envelope or other binary mass ejection mechanisms are likely to only occur in very tight systems (common envelope requires the expansion of the star, and helium stars do not expand much in most stellar evolution calculations), so such systems will start in tight binaries and only become tighter (separations within a few Roche limits).

Carbon/oxygen stars, the progenitors of Type Ic binaries, are more compact than He-stars and, hence, can produce tighter binaries. Hence, the BH spins are higher for these CO stars. Hydrogen common envelope scenarios will produce a wide range of separations between the helium core and its companion star. Only a small fraction of these common envelope inspirals will produce the tight binaries needed to produce fast-rotating cores. This is because hydrogen envelopes are extended and easily ejected in a common envelope. Most of the helium stars in these systems will not be spun up through tidal locking. CO cores are in a different situation. Helium stars are less extended. If a helium binary mass ejection occurs, the binary will be tight. The question for this scenario is whether helium binary mass ejections even occur. CO cores can be produced simply through mass loss in strong Wolf–Rayet winds, but this would only occur for the most massive-star observations, and current supernova observations argue against such a scenario (see A. Gilkis et al. 2025, and references therein). For our discussion, we will assume such helium common envelopes can occur.

3. Magnetar Energies

Magnetar engines tap the rotational energy in the newly formed NSs to power emission or a jet. With the spin periods from Section 2, we can calculate this energy. The moment of inertia for neutron stars depends upon the equation of state (A. Worley et al. 2008), but all estimates of the moment for an NS ($I_{\rm NS}$) are within a factor of 2 of:

$$I_{\rm NS} = 10^{45}(M_{\rm NS}/M_\odot)\,{\rm g\ cm^2} \quad (9)$$

where $M_{\rm NS}$ is the NS mass. The corresponding rotational energy ($E_{\rm rot}$) is:

$$E_{\rm rot} = 5 \times 10^{50}(\omega/1000\ {\rm Hz})^2\ {\rm erg} \quad (10)$$

where ω is the angular velocity. An NS with a spin period of 1 ms has a total of 2×10^{52} erg.

The maximum spin period of NSs is limited by instabilities in the NS. The onset of these instabilities occurs when the rotational energy exceeds 14% of the potential energy of the neutron star (S. L. Shapiro & S. A. Teukolsky 1983):

$$\beta = E_{\rm rot}/|W| > 0.14 \quad (11)$$

where

$$|W| = GM_{\rm NS}^2/r_{\rm NS} \approx 5 \times 10^{53}\ {\rm erg} \quad (12)$$

and, for the neutron star mass and radius, we have $M_{\rm NS} = 1.4\,M_\odot$, $r_{\rm NS} = 10$ km, respectively. These instabilities place an upper limit on the energy available for a magnetar of $\approx 7 \times 10^{52}$ erg. But other instabilities can further reduce the maximum total energy. For example, at extremely high spin rates, Rossby waves can develop, driving the total rotational energy down another order of magnitude (W. C. G. Ho & D. Lai 2000; D. Lai et al. 2001). At a fixed angular momentum, the rotational energy in the proto-neutron star increases as it becomes more compact. If the magnetar-strength magnetic fields develop when the proto-neutron star is still hot and extended, it can lose its angular momentum before the rotational energy reaches its peak. For a

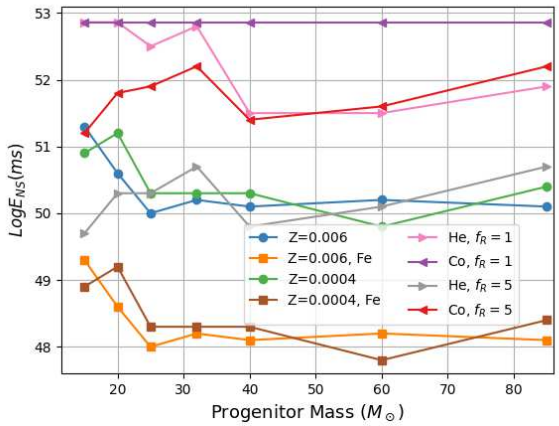

Figure 6. Available rotational energy for neutron stars in stellar collapse as a function of zero-age main-sequence mass. Because the neutron star only exists in its hot, extended state for the BH-forming, progenitor masses above 25 $M_\odot$ can only have weak magnetars.

given amount of total angular momentum ($J_{\rm tot}$), the total rotational energy is inversely proportional to the square of the radius:

$$E_{\rm rot} = 1/2 I_{\rm NS}\omega^2 = 1/2 J_{\rm tot}^2/I_{\rm NS} \propto J_{\rm tot}^2/r_{\rm NS}^2. \quad (13)$$

A hot NS has a radius roughly 3 times that of a cold NS. At this point, the total rotational energy is roughly 10 times lower than the NS will have when it cools. For BH-forming systems, this is the only magnetar energy reservoir, making it difficult for magnetar engines to have much power for these systems. The most powerful magnetars are likely to be produced in NS-forming systems where the magnetar-like fields are not completely formed until the NS cools.

If Rossby waves develop, the rotational energy available to magnetars would be low. But viscous damping of these waves can limit the amount of angular momentum lost to these waves (L. Bildsten & G. Ushomirsky 2000). If we ignore Rossby instabilities, focusing only on other (e.g., bar) instabilities, we can estimate the maximum rotational energy available for magnetar engines. Figure 6 shows the range of energies for both single stars and binary systems. For single stars, the rotational energies available for magnetar engines lie below $\sim 10^{51}$ erg. For binary systems, particularly close CO stars, this rotational energy reaches the upper limit available.

From these results, we can identify trends in lGRBs and their associated SNe. For our single star models assuming coupling caused by the Tayler-Spruit dynamo (H. C. Spruit 2002), the magnetar energies are typically below 10^{50} erg. The most powerful magnetars arise from binaries. A broad range of CO binaries achieve rotational energies near the maximum value derived above. Only the tightest He star binaries will have the energies to produce normal GRBs. Under these progenitors, we would expect most GRB-associated SNe to be classified as type Ic. However, this progenitor also argues that the most energetic magnetars should occur from lower-mass progenitor stars and we'd expect no significant metallicity or redshift dependence under this engine. The only effect of metallicity would be the fact that the initial mass function flattens with lower metallicity. Under this engine, the rate of GRBs as a function of star formation should decrease with decreasing metallicity and increasing redshift (see Section 5.4).

4. BHAD Accretion and Energies

BHAD engines rely, first and foremost, upon the formation of an accretion disk. Models with modest coupling (e.g., our Kepler models) are just at the boundary between insufficient and sufficient angular momentum to produce a disk. A number of mechanisms have been discussed to extract energy from accreting BHs (C. L. Fryer et al. 2019), tapping energy either from the energy in the disk or rotational energy of the BH. But all of these require an accretion disk either as an energy source or as a mediator. To understand BH accretion disk engines, we must first understand the accretion rate and accretion disk evolution.

Accretion rates and durations provide insight into the properties of lGRBs. The timescale of disk accretion is set by the duration at which the disk is fed by the collapsing star and the accretion timescale of the disk. The disk feeding timescale is often approximated by the freefall time of material collapsing onto the compact object (C. L. Fryer et al. 2019). This freefall time ($t_{\rm ff}$) is set by the enclosed mass within that radius corresponding to the BH mass ($M_{\rm BH}$) and the position of the free-falling material (r) at the time of collapse:

$$t_{\rm ff} = \pi r^{3/2}/\sqrt{8GM_{\rm BH}}. \quad (14)$$

This timescale gives the approximate time at which the material forms in a disk.

The disk accretion timescale can be estimated from an α-disk model (R. Popham et al. 1999). In the alpha-disk prescription, the accretion timescale ($t_{\rm acc}$) of the disk is set to the orbital period ($P_{\rm disk}$) of matter in the disk divided by an efficiency parameter (α):

$$t_{\rm acc} = P_{\rm disk}/\alpha = 2\pi r_{\rm disk}^{3/2}/(\alpha\sqrt{GM_{\rm BH}}) \quad (15)$$

where $r_{\rm disk}$ is the radial extent of the disk set by the specific angular momentum, $j(r)$, in the star:

$$r_{\rm disk} = j(r)^2/(GM_{\rm BH}) \quad (16)$$

and the corresponding accretion time through the disk in terms of angular momentum is:

$$t_{\rm acc} = 2\pi j^3(r)/\alpha/(GM_{\rm BH}^2) = 3.9s\left(\frac{j(r)}{10^{17}\ {\rm cm^2\ s^{-1}}}\right)^3\left(\frac{0.01}{\alpha}\right)\left(\frac{3M_\odot}{M_{\rm BH}}\right)^2. \quad (17)$$

For our binary models, we assume the duration of the jet is the combination of the freefall and accretion timescales. For the fastest rotating models, this time is set by the disk accretion timescale, but for the more compact cores, the timescale is close to the freefall time. The corresponding accretion rates using these accretion parameters for a range of Kepler pre-collapse progenitors (S. E. Woosley et al. 2002) are shown in Figure 7.

For our smallest BH-forming systems, the accretion rate can extend out to 1000 s, potentially explaining the ultra-long GRBs (see Section 6). The accretion timescale shortens for wider binaries. The top panel of Figure 8 shows the accretion rate as a function of time for binaries at different separations. As the binary becomes wider, the time to form a disk gets longer.

It is possible that the jet-driven explosion will disrupt the star (A. I. MacFadyen & S. E. Woosley 1999), shortening the accretion duration. But there are also methods to extend the accretion timescale. One way to extend the accretion phase,

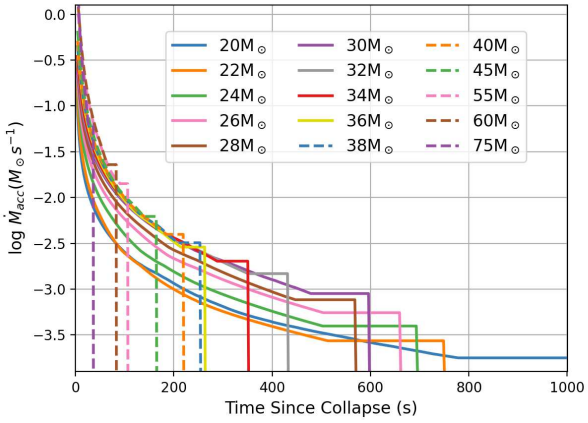

Figure 7. Disk accretion rate as a function of time for tight-binary ($f_R = 1.0$) systems with zero-age main-sequence masses ranging from 20–75 $M_\odot$. The more common, 20 $M_\odot$ progenitors continue to accrete for over 1000 s.

and hence drive the engine longer, is to argue that the accretion process is much more complex than the α-disk model suggests. One such process is the magnetically arrested disk (MAD) where a poloidal field produced in the collapse or wound up in the disk creates enough pressure at the event horizon to halt accretion (for an overview, see N. M. Lloyd-Ronning et al. 2016). But MAD disks are unlikely to extend the duration of the accretion disk considerably. Alternative mechanisms have been proposed to extend the emission relying on dense or baryon-loaded ejecta (H. J. van Eerten 2014; P. C. Duffell & A. I. MacFadyen 2015). Another way to extend the disk accretion timescale is to tap the angular momentum in the BH to prop up the disk (M. H. P. M. van Putten 1999). We will discuss the role of disk durations and their impact on GRB signals in Section 6.

For many BHAD mechanisms, the power of the accretion disk is set by the kinetic energy in the disk which, in turn, depends upon the structure of the disk (accretion rate) and BH spin. R. Popham et al. (1999) calculated these disk properties, providing an estimate of the jet energy as a function of BH spin and accretion rate. These results assumed that the strength of the magnetic field was limited by the energy in the disk (i.e., the magnetic field energy density could not exceed the disk thermal energy density). Fitting to these models, A. Heger et al. (2003) developed a formula for the jet power ($L_{\rm jet}$):

$$L_{\rm jet} = \frac{f_{\rm jet}}{0.01} 10^{50} 10^{0.1/(1-a_{\rm BH})-0.1} \left(\frac{3M_\odot}{M_{\rm BH}}\right)^3 \frac{\dot{M}_{\rm disk}}{0.1\ M_\odot\ {\rm s}^{-1}} {\rm erg\ s}^{-1} \quad (18)$$

where $\dot{M}_{\rm disk}$ is the accretion rate as shown in Figure 7, and $f_{\rm jet}$ is a factor roughly describing the efficiency. Because the energy in the disk decreases with larger BH radii, this mechanism decreases with BH mass.

The original R. D. Blandford & R. L. Znajek (1977) study predicts a jet power that is much less sensitive to the disk energy density:

$$L_{\rm jet} = 3 \times 10^{51} a_{\rm BH}^2 \frac{\dot{M}_{\rm disk}}{0.1\ M_\odot\ {\rm s}^{-1}} {\rm erg\ s}^{-1}. \quad (19)$$

Other studies follow this same trend, predicting extremely powerful jet engines. O. Gottlieb et al. (2023) argued that the

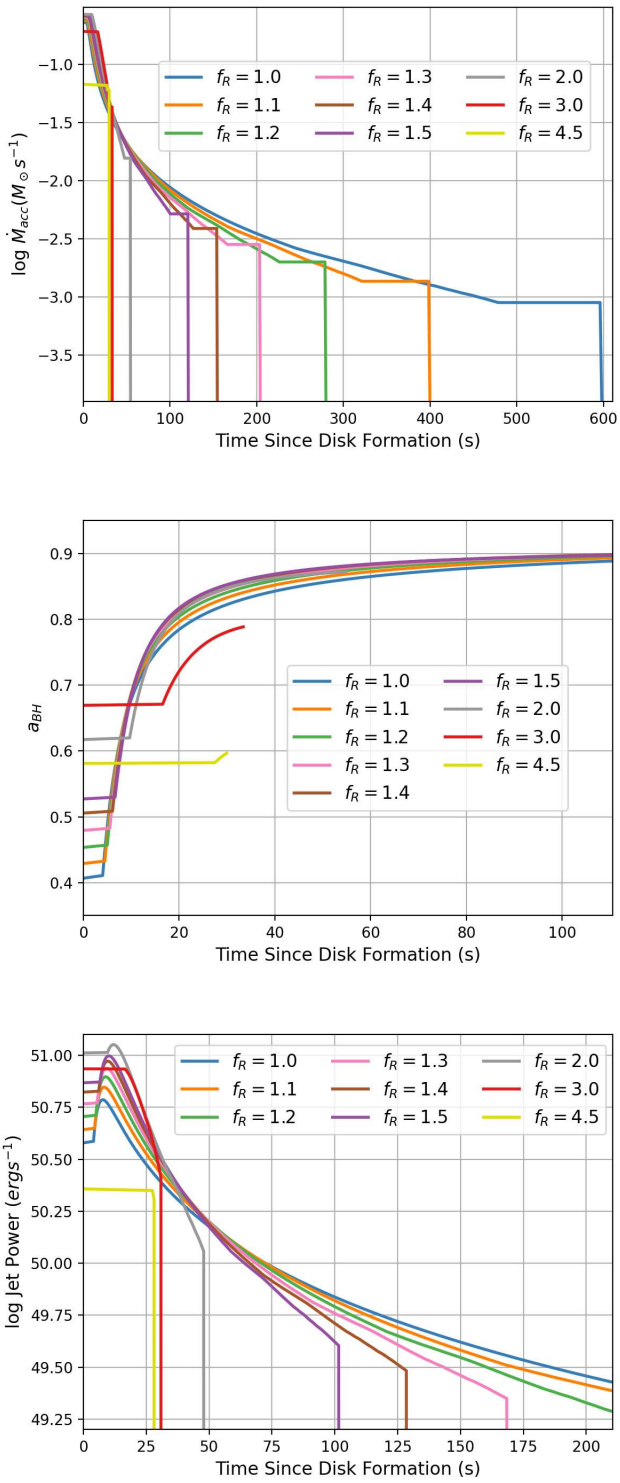

Figure 8. Top panel: accretion rate vs. time after the formation of the disk for a 30 $M_\odot$ zero-age main-sequence progenitor as a function of time after the formation of the disk. Disk formation occurs later for wider binaries. Middle panel: corresponding black hole spin rate as a function of this time. Bottom panel: GRB jet power as a function of time using Equation (19).

jet power is:

$$L_{\rm jet} = 2 \times 10^{53} (1.063 a_{\rm BH}^4 + 0.395 a_{\rm BH}^2) \frac{\dot{M}_{\rm disk}}{0.1\ M_\odot\ {\rm s}^{-1}} {\rm erg\ s}^{-1}. \quad (20)$$

For this latter jet prescription, we can achieve high energies even for slowly rotating BHs. The angular momentum

requirement for this engine is not set by the energy requirements of the GRB, but the angular momentum required to produce a disk.

We use Equation (19) to determine the power in the jet in Figure 8. The variation in jet powers is less than the variation of observed luminosities of GRBs (M. Maistrello et al. 2024). Without an accepted model for the conversion of jet energy to gamma-ray luminosity, making a direct comparison between this jet power and gamma-ray observations is problematic. For example, the variation in the luminosity could depend on instabilities in the disk (e.g., A. Ł. Lenart et al. 2025) and/or turbulence in the jet (B. Zhang & H. Yan 2011), neither of which are accounted for in our simple model using Equation (19). But the total energy released should be similar. For the wider binaries, the disk forms later, but the BH has accreted more, so the spins are, if anything, higher. The final angular momentum does not reach the high values ($a_{\rm BH} > 0.9$) that our tight binaries achieve. The resulting power in these systems is weaker and has a much shorter duration. Our short-duration disks can either form from massive progenitors (producing strong explosions) or wide binaries (producing weak explosions). Although our ultra-long durations can have initially strong GRB jet power, the late-time power should be much less.

The jet drives a shock through the star, and this shock can drive the explosion of the star (A. I. MacFadyen & S. E. Woosley 1999). Winds from the disk drive an outflow that can also contribute to the explosion energy. The fraction of the disk mass ejected in this wind can be anywhere from 1%–30% of the disk mass, and the velocities are within a factor of a few of the escape velocity. Depending on the properties of the disk, the disk wind ejecta can carry considerable energy (more than 10^{51} erg), and the SNe produced in these massive-star GRBs are driven by a combination of this disk wind and jet energies. The disk winds will dominate the nucleosynthetic yield produced during the explosion itself (we will discuss this in Section 5.1).

5. Observational Features

The specific progenitors for highly rotating magnetar, NSAD, and BHAD models will have observational features that can allow us to distinguish between these strong SN explosions and normal SNe. With more detailed studies, we may be able to distinguish between these different high-spin engines. Here, we discuss a set of potentially distinguishing features of these engines.

5.1. Nucleosynthetic Yield Signatures

The mechanisms producing the nucleosynthetic yields from core-collapse stars with convective-driven explosions can be categorized into three components: (1) isotopes produced in burning layers during stellar evolution, (2) isotopes produced in the convective region (typically iron peak elements), and (3) isotopes produced in the explosive shocks (primarily producing a range of alpha-chain elements). Similarly, models invoking accretion disks also have three production components: (1) isotopes produced in burning layers during stellar evolution, (2) isotopes produced in the accretion disk and ejected in a viscosity-driven wind (typically iron peak elements), and (3) isotopes produced as the wind ejecta plows through the star.

A few general comments guide the nature of the yields in these explosions. The production of *r*-process elements requires the collapsing stellar material to become neutron-rich. Although electron capture can occur both in the convective and disk-driven engines, neutrinos from the NS tend to reset this neutronization and, for most models, these explosions do not produce elements beyond the iron peak or the first *r*-process peak. Even for BH-forming core-collapse stars, the densities and temperatures in the disk are typically not sufficiently high to drive significant deleptonization (R. Popham et al. 1999; R. Surman et al. 2006) to produce significant amounts of heavy *r*-process and recent results arguing that *r*-process production in these events is typically hampered by numerical artifacts (J. M. Miller et al. 2020). The amount of deleptonization is easily estimated as a function of the accretion rate. Figure 7 shows the disk accretion rates as a function of progenitor mass and progenitor rotation. Based on the Popham et al. disk models and their predicted neutrino luminosities (R. Popham et al. 1999), we can estimate the deleptonization within the disk:

$$dY_e/dt \approx N_{\rm p}/(L_{\nu_e}/\epsilon_{\nu e})t_{\rm acc} \quad (21)$$

where $N_{\rm p}$ is the number of protons, L_{ν_e} is the neutrino luminosity from electron capture, $\epsilon_{\nu e}$ is the neutrino energy, and $t_{\rm acc}$ is the accretion timescale. The electron capture luminosity is highly sensitive to the temperatures in the disk ($L_{\nu_e} \propto T^6$ where T is the temperature). Because of this, accretion rates above 0.5–1 $M_\odot\,{\rm s}^{-1}$ are needed to reduce the electron fraction below 0.4. As such, strong deleptonization is limited to NS mergers (e.g., J. M. Miller et al. 2019) and our most massive stars (low-metallicity stars above $\sim$60 $M_\odot$; see Figure 7).

Because of this, we will focus our nucleosynthetic yield study on the production of alpha elements up to the iron peak from our disk yields. In these disk-driven explosions, disk winds dominate the production of heavy (iron peak) elements. The production of these elements depends sensitively on the maximum radius of the disk (more compact disks eject less mass). Using the low-entropy disk models from M. A. R. Kaltenborn et al. (2023), we calculate the disk yields and combine them with the ejecta from stellar evolution. The total yields as a function of the extent of the accretion disk are shown in Figure 9. The ^{56}Ni yield, one of the power sources for the SN transients from these explosions, varies by an order of magnitude depending up the disk radius. If this is the only energy source, the associated supernova luminosities from these explosions can range over an order of magnitude. However, as we shall discuss below, these transients can also be powered by shock heating.

5.2. Circumstellar Medium

The circumstellar medium for our tidally locked binaries is determined by the mass transfer events that produce the tight binaries in our magnetar, NSAD, and BHAD progenitors. This explosive mass loss will produce heterogeneities in the circumstellar medium that may be observed in the resulting transient emission. Shock interactions with the ejecta from the last mass transfer phase, the removal of the helium envelope, are likely to have the most dramatic effect on the transient emission. Here we estimate the properties of this mass loss based on stellar evolution models.

Table 1
Final Binary-induced Mass-loss Phase is Likely to Occur between Helium Depletion (He Dep) and Carbon Ignition (C Ign)

Engine	$\text{Time}_{\text{HeDep}}$	$\text{Time}_{\text{CIgn}}$	$R_{\text{shell,HeDep}}$	$R_{\text{shell,CIgn}}$	$T^{\text{HeDep}}_{\text{interaction}}$	$T^{\text{CIgn}}_{\text{interaction}}$	M_{ejecta}
BHAD	$\sim 10^4$ yr	1–10 yr	$\sim$10 pc	0.001–0.01 pc	200 yr	7–70 days	2–10 $M_\odot$
Magnetar/NSAD	1–3 $\times$ 10^4 yr	10–1000 yr	$\sim$10–30 pc	0.01–1 pc	200–600 yr	70–700 days	0.5–2 $M_\odot$

Note. Assuming an common envelope ejecta velocity of 1000 km s^{-1}, we infer the position of this ejecta shell.

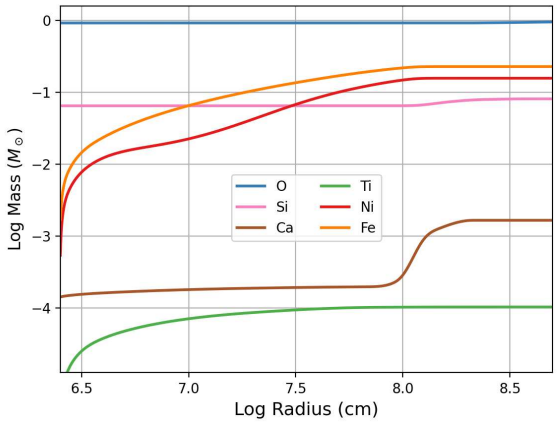

Figure 9. Abundances from a disk wind as a function of the extent of the disk. This assumes that the wind ejects matter along most of the disk (using the model from M. A. R. Kaltenborn et al. 2023).

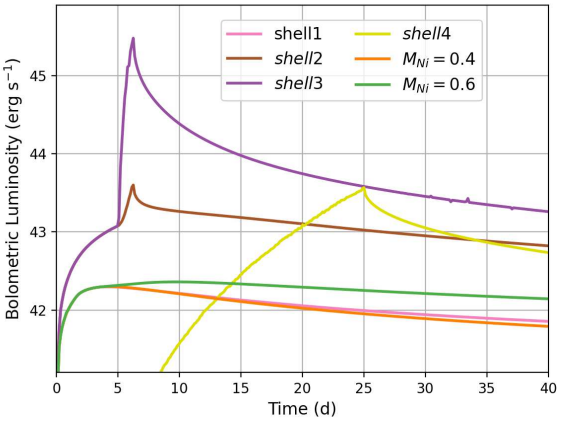

Figure 10. Comparing bolometric light curves from high nickel yield Ic-BL and low nickel yield Ic-BL with weak shocks. We defer a more detailed study of the spectra and broadband light curves to an upcoming paper (C. L. Fryer & D. A. Fryer 2025).

We estimate the ejecta mass by assuming that the final mass transfer phase occurs somewhere between the end of core helium burning to the beginning of carbon ignition. For this study, we use the timescales and helium-shell masses inferred stellar evolution models reviewed in S. E. Woosley et al. (2002). Table 1 shows the range of time prior to collapse of the end of helium burning (He depletion) and carbon ignition. The timescales differ for NS and BH-forming stars. The more-massive stars that form BH systems have shorter timescales and more-massive ejecta masses than those forming NSs.

If we assume an common envelope ejecta velocity of $\sim$1000 km s^{-1} (roughly the escape velocity for helium stars), we can infer the rough position of this binary-interaction ejecta and the timescale at which the hypernova shock would hit the shell. If the binary mass transfer occurs at the end of helium burning, the shell will be sufficiently far from the star that it will not affect the light curve. But, especially for the BHAD engine, if the mass outflow occurs at the onset of carbon or oxygen burning, we expect strong shock interactions. Some shock interactions should be expected as the hypernova ejecta propagates through the clumpy Wolf–Rayet winds (C. L. Fryer et al. 2020).

If the mass ejection occurs during helium depletion, 10,000 yr before collapse, the shell of ejecta will integrate within the ISM, and it will be difficult to detect evidence for the mass loss. However, if the mass ejection occurs after carbon ignition, the SN/jet shock will hit the shell within 7–70 days. The densities of these shells are on par with the explosive ejecta, 10^{-16}–10^{-12} g cm^{-3}, and the shock in the interaction will significantly decelerate the shock, converting kinetic energy into thermal energy. In these scenarios, shock heating dominates the light curve. It is possible that spectral features may allow us to distinguish different heating sources. Simple models like those presented here predict very different properties of the light curves and spectra but, as is often the case in nature, reality is much more complex. Distinguishing these models may be very difficult. One approach is to look at late-time observations to distinguish the energy sources (N. Afsariardchi et al. 2021; J. Sollerman et al. 2022; Ó. Rodríguez et al. 2024).

Figure 10 shows the SN light curves for a select set of ejecta properties and nickel masses and mass distributions. For the inner shells, it will be difficult to distinguish the peak emission from light curves powered by ^{56}Ni decay. If the shocks are strong, shock interactions can make extremely bright SNe. For shells that are sufficiently far out that the shock interaction with the shell occurs 20–30 days after the launch of the explosion, we expect a double-peaked light curve. Observations of or lack thereof this second peak will place constraints on our CO binary model. Although there are some Ic-BL that show evidence of shock interactions (A. Corsi et al. 2014; L. J. Wang et al. 2019), the simple models used to infer the properties of the mass ejection (using assuming a wind-like mass loss) can produce inaccurate conclusions. The structure of this ejecta, particularly the inhomogeneities, can alter the emission from these shock interactions (C. L. Fryer et al. 2020). A broad wavelength coverage (from radio to X-ray) of the emission will likely constrain the structure, but a better understanding of shock interactions to determine the extent of these constraints.

5.3. Gravitational Waves

The collapse of mildly rotating stars does not lead to strong gravitational-wave emission. The gravitational-wave signal produced by the standard, convective-engine paradigm behind core-collapse SNe is a strong probe of the convection and its growth, but the gravitational-wave amplitudes are typically $<10^{-22}$ Hz$^{1/2}$ at 10 kpc (for a review, see C. L. Fryer & K. C. B. New 2011). Even for next-generation detectors like

Cosmic Explorer (D. Reitze et al. 2019), a 5σ–10σ observation is limited to a distance of $\sim$1 Mpc, our Local Group.

Modestly rotating models, e.g., our rotating Kepler models and wide separation CO- or He-core binaries, lead to an aspherical collapse that will produce signals that are 5–10 times higher amplitude than slowly rotating models. A small fraction of these rotating models may be detectable out to the Virgo cluster by Cosmic Explorer.

But, as we discussed with our magnetar engine models, our tightest CO-star binaries will have such fast spins that they will undergo dynamical instabilities. For bar-mode instabilities, the requirement on the spin is: $\beta = E_{\rm rot}/|W| > 0.27$. Such high values for β are achievable in our binaries with orbital separations near the Roche limit. These systems would be detectable by Cosmic explorer beyond 100 Mpc (C. L. Fryer et al. 2023).

Although a lack of a gravitational-wave detection of a Virgo-cluster SN would not preclude a tight CO-star binary progenitor, a detection would prove that high-spin systems like those made by our tight binaries are produced.

5.4. Dependence on Metallicity and, hence, Redshift

For our different engine scenarios, the fraction of massive stars that form GRBs is affected differently by the metallicity, arguing for a different evolution with redshift. The rate depends both on the shape of the initial mass function and the wind mass loss (C. L. Fryer et al. 2022). There is growing evidence that the initial mass function begins to flatten as the metallicity drops below 0.01–0.1 $Z_\odot$ (S. Chon et al. 2021). As it flattens, the fraction of BH-forming systems increases. In addition, mass loss from winds decreases with decreasing metallicity. Weaker winds also allow more BH-forming systems to form. For our binary progenitors, we expect the number of BHAD explosions to increase with decreasing metallicity and, hence, increase with redshift.

In contrast, NS engines (NSAD, magnetar) are produced by lower-mass stars (less than $\sim$20 $M_\odot$), which depend much less on mass loss. Because the relative fraction of these stars decreases as the initial mass function flattens, under the tidally locked progenitor mechanism, we'd expect the rate of explosions from these engines to decrease with decreasing metallicity and hence with increasing redshift.

But many questions remain unanswered on the metallicity dependence of GRBs. For example, the apparent lack of metallicity evolution in GRB hosts (J. F. Graham et al. 2023) points toward missing aspects in our model, likely due to our lack of understanding of stellar and binary evolution.

5.5. Failed versus Strong Jets

An important open question in our understanding of the lGRB-SN connection is whether all Ic-BL SNe are produced by jet-driven engines where the difference between lGRBs and Ic-BL SNe without GRBs is determined solely by the Lorentz factor of the jet either because the jet was weak when launched or the jet was unable to clean out a funnel because of its short duration and baryon loading slows the jet (K. Nomoto et al. 2001, 2007; M. Modjaz et al. 2008, 2020; D. Lazzati et al. 2012). In our tight-binary model, depending on the binary separation, we produce different-sized disks (which vary both the jet power and duration). The binary separation coupled with the mass of the collapsing star can explain the transition between lGRBs, LLGRBs, and Ic-BL SNe without GRBs based on the correlation between accretion rate and jet power. The most powerful jets produce lGRBs. These lGRBs would be produced by our tightest binaries and more-massive BH-forming stars. This high energy may also affect the associated SNe. The current set of observed Ic-BL SNe accompanying lGRBs is very luminous. LLGRBs would be produced by wider binaries, preferentially from the low-mass BH-forming stars. Ic-BL SNe without GRBs would be produced by our least-powerful jets from the widest binaries and preferentially low-mass progenitors.

Although we just described some basic trends with mass, without a more detailed understanding of the mass-loss mechanism forming CO binaries, it is difficult to make strong claims on these masses or rates. Our poor understanding of the jet engine and its propagation through the star also prevents solid constraints on the properties of the Ic-BL SNe produced in all of these cases. Here we differentiate three scenarios for tight-binary, BHAD engines:

1. Massive stars in the higher-mass range (above $\sim$30 $M_\odot$) in tight binaries produce strong jets with a range of durations. If the disk winds dominates the SN energy, more-massive stars will produce SNe with higher mass, but higher total energy. In this scenario, more-massive stars will produce more-massive and higher-energy Ic-BL SNe. Wider binaries will produce weaker explosions, producing a range of energies from the same progenitor mass.
2. Massive stars on the lower-mass range (roughly in the 20–30 $M_\odot$ range) produce weak jets (either LLGRBs or Ic-BL SNe without GRBs). If these explosions are equally efficient at tapping jet energy to drive the SNe, they will be weaker than GRB-SNe. But it is likely that these jets inject more of their energy into their host stars, and hence, these SNe could have a range of energies.
3. Wide binaries will also produce weaker GRBs and Ic-BL SNe without GRBs. The weakest explosions will be lower-mass progenitors.

The extent of the broad lines may be able to help us distinguish between these different scenarios. The violent mass loss required in the formation of these tight binaries suggests that shock heating could dominate the light curve. If so, the luminosity of the SN depends more on the circumstellar medium than it does on the energy in the SN explosion. In this case, broadband wavelength coverage (radio, ultraviolet, X-ray) could provide clues to the nature of the shock interactions. Nonetheless, any trends in the SN and GRB properties can be used to provide clues into both the progenitor binary-induced mass loss and jet formation.

5.6. Jet-engine Duration and Baryon Loading

The initial jet is typically baryon-loaded as it pierces through the star (A. I. MacFadyen & S. E. Woosley 1999). The jet engine requires some time (some factor roughly equal to the jet transit time) to clear out a funnel to achieve high Lorentz factors (prior to clearing out this funnel, the jet gains mass, a.k.a., baryon loaded). Although the front of the jet can accelerate at breakout (S. A. Colgate 1968; J. C. Tan et al. 2001), if it is baryon loaded, it cannot reach high Lorentz factors.

For our C/O cores, the transit time of the jet through the star is $<$1 s, much shorter than the BHAD engine lifetimes. For the

Table 2
Ultra-long GRBs and Associated Properties

Burst	Redshift	Observed Duration	Rest-frame Duration	E_{iso}	L_{iso}	References
GRB 220627A	3.084	3700	900	2.30E+54	1.30E+53	D. Frederiks et al. (2022)
GRB 101225A	0.847	1377	800	2.70E+52	9.50E+52	A. J. Levan et al. (2013)
GRB 121027A	1.773	5700	2000	1.10E+53	1.20E+52	A. J. Levan et al. (2013); A. Lien et al. (2016)
GRB 091024A	1.0924	1200	600	3.50E+53	1.00E+52	D. Gruber et al. (2011); F. Virgili et al. (2013)
GRB 141121A	1.469	∼1500	∼620	8.00E+52	1.00E+51	S. Golenetskii et al. (2014); A. Cucchiara et al. (2015)
GRB 170714A	0.793	∼1030	∼570	3.50E+52	8.30E+50	A. Lien et al. (2016); D. M. Palmer et al. (2017)
GRB 111209A	0.677	10000	6000	6.00E+53	8.10E+50	S. Golenetskii et al. (2011)
GRB 130925A	0.347	4500	3300	1.50E+53	4.00E+50	S. Golenetskii et al. (2013)
GRB 090417B	0.345	2130	1600	4.50E+51	1.50E+50	S. T. Holland et al. (2010)

Note. Energetics values are either taken from bolometric values in papers or calculated from available flux/fluence and spectra values for this work.

BHAD engine, our tight CO binaries should be able to clear out the jet region, allowing for the creation of relativistic jets. For more extended binaries, predominantly He cores, we can have shorter-lived and weaker jets that may fail to reach high Lorentz factors.

Many models assume that the BHAD GRB duration is set by the accretion timescale of the disk. Under this engine, our most massive progenitors or systems in wider separations would produce shorter-lived GRBs. To produce longer-duration GRBs, we'd be limited to tight binaries with lower-mass CO cores or would have to invoke models like that of M. H. P. M. van Putten (1999) to extend the disk duration. However, the duration for some models producing the gamma-ray emission may not be constrained by the jet engine (B. Zhang & H. Yan 2011). In such a scenario, the duration of the jet engine is not an important constraint.

The duration of the engine dictates how baryon-free the jet becomes (determining the uppermost Lorentz factors of the jet). This jet-engine duration is also linked to the duration of the GRB. For all prescriptions of the jet-driven engines, the jet energy is proportional to the accretion rate. The power of the jet can decrease dramatically with decreasing accretion rate. For our more-massive stars, the duration of the jets is limited to $<$100 s, but lower-mass BH-forming progenitors can form longer-duration engines. But, under the BHAD engine, these engines will be weaker beyond 100 s. Observations indicating that the jet weakens at late times, $\propto t^{\sim -1}$, would support a lower-mass BH-forming progenitor.

6. GRB Constraints

It has already been noted that observations indicating that lGRBs occur preferentially in low-metallicity, star-forming galaxies (A. S. Fruchter et al. 2006) already argue that the engine under our tight-binary progenitor must be the BHAD engine. But we can use additional observations to determine the role of the tight-binary progenitor scenario in explaining a wide range of GRB subclasses, including ultra-long and low-luminosity GRBs.

Note that we place GRBs 061208 and 100316D into the low-luminosity GRB class despite meeting our criterion of ultra-long GRBs, for reasons explained below.

6.1. Ultra-long GRBs

Ultra-long GRBs have been discussed as possibly arising from a unique progenitor compared with the broader lGRB population (e.g., A. J. Levan et al. 2013). While the definition of ultra-long is imprecise, we adopt the definition of an observed duration in excess of 1000 s. Some papers suggest ultra-longs are merely the extreme tail of the long population (e.g., F. Virgili et al. 2013). Other papers invoke alternative models that include a minor body falling onto an NS (S. Campana et al. 2011), a helium star–NS merger (C. C. Thöne et al. 2011), the collapse of a blue supergiant (B. Gendre et al. 2013; D. Nakauchi et al. 2013), a magnetar engine (B. Gompertz & A. Fruchter 2017), tidal disruption events (K. Ioka et al. 2016), and other unique origins (D. Kann et al. 2019).

These nonstandard scenarios are typically invoked because it is thought to be difficult to explain the extreme length of prompt duration with a Wolf–Rayet progenitor. This relies on two assumptions: (i) that the emission duration is of similar order as the accretion time, and (ii) that the accretion time for a collapsar is effectively the freefall time. We maintain the former, which is a prediction of internal shocks and some other prompt GRB emission models (B. Zhang 2018). The model described here challenges the second consideration, in some cases.

From Figure 7, we find that the lowest-mass BH-forming progenitors in tight binaries produce the longest-lived accretion disks (due to the high angular momentum where the disk accretion time far exceeds the freefall time). The accretion rates in these disks steadily decrease with time, and we expect lower jet powers as the ultra-long GRBs evolve. Lower-mass progenitors should produce weaker jets on average. We also expect ultra-long bursts to be less sensitive to metallicity than normal GRBs. Finally, the low-mass CO stars in these progenitors should be observed in any associated supernova with the lower masses tending to produce shorter supernova transients (if all else, e.g., shock heating, were equal).

We can compare these predictions to the current observational sample of ultra-longs, compiled from the literature and summarized in Table 2. While the definition of ultra-long is imprecise, we adopt the definition of an observed duration in excess of 1000 s. For duration comparison with our accretion timescales, we compare with the rest-frame duration.

Since luminosity is key, this restricts our sample to events with measured redshift. We compare the observed peak luminosity of our ultra-long sample to the broad sample of bursts reported in E. Burns et al. (2023), which were detected by the Fermi Gamma-ray Burst Monitor (GBM; C. Meegan et al. 2009). Using a two-sample Anderson–Darling test, we find that they are incompatible at $>$99.9% significance. While this is an imperfect test because of differential selection functions for different gamma-ray burst monitors, only two

ultra-longs have peak luminosities above the median measured $L_{\rm iso}$ of $\sim 5 \times 10^{52}$ erg. We thus confirm that these events appear to arise from jets with lower jet power, as compared with the broader population.

The highest $L_{\rm iso}$ ultra-long GRB is GRB 220627A, with a rest-frame duration of 900 s and a peak luminosity at the 70th percentile. However, the ultra-long duration arises from a period of very weak emission, with large spikes ending only 300 s after the start (in the rest frame), which is consistent with our low-jet power picture at late times. There are a few GRBs whose overall rest-frame duration exceeds 1000 s; however, the only GRBs with impulsive behavior beyond this duration are GRBs 111209A, 130925A, and 090417B, with peak luminosities at the 1st percentile of the GBM sample. Thus, the durations and luminosities of ultra-long GRBs are consistent with model expectations.

Thus far, there are not dedicated studies on comparing a sample of ultra-long GRB host-galaxy metallicities against the broader population. A. J. Levan et al. (2013) studied three ultra-long GRBs and noted the host galaxies may differ from the wider sample, but do not flag metallicity as an obvious difference. P. Schady et al. (2015) found a supersolar metallicity host for GRB 130925A, which is the second-longest rest-frame duration GRB observed so far. Thus, this test is interesting but does not provide conclusive evidence either way, and motivates future host-galaxy characterization of ultra-long GRBs.

Similarly, there are very few ultra-long GRBs with associated supernova. GRB 111209A, the longest GRB ever observed, has the associated SN 2011kl, which appears more luminous than typical GRB supernovae (D. Kann et al. 2019). Precise statements will require prioritized follow-up of future ultra-long GRBs to characterize their supernova.

6.2. Low-luminosity GRBs

An additional GRB type that is discussed as a separate class but may be part of a continuum are low-luminosity GRBs. They appear to arise from collapsars, being followed by Ic-BL SNe, but the specific cause of the lower GRB luminosity is not known. These events may be caused by off-axis jets akin to the low-luminosity prompt GRB 170817A (B. P. Abbott et al. 2017), but this is certainly not always the case (e.g., R. Margutti et al. 2013). Alternatively, the jet may barely escape the progenitor star which could result in a typical GRB event with lower overall power. Some of these may even fail to escape the star and be fully choked within them, producing a prompt high-energy signal powered by a quasi-spherical shock breakout rather than internal dissipation of the energy within a jet. Indeed, some low-luminosity GRBs appear similar with such an outcome (E. Nakar et al. 2012), but not all. The lowest-luminosity events include GRBs 061208 and 100316D, which appear to have very smooth, comparatively soft prompt emission, being consistent with expectations of shock breakout (e.g., S. Campana et al. 2006; R. Margutti et al. 2013).

In addition to being followed by Ic-BL SNe, low-luminosity GRBs prefer host-galaxy metallicities similar to lGRB SNe, being much lower than the metallicities found in typical Ic SNe (M. Modjaz et al. 2020). This is strongly suggestive of a common progenitor of cosmological lGRBs. The non off-axis scenarios are all consistent with a common formation channel where the ultimate jet is weak, compared to cosmological GRBs.

7. SN Constraints

SN observations can further constrain the nature of the progenitor and of the engine (or engines) responsible for the explosions. Metallicity dependence for both Ic-BL associated with GRBs and those without GRBs can provide key insight into the engines and progenitors. M. Modjaz et al. (2020) measured the gas-phase metallicities at the sites of 28 Ic and 14 Ic-BL SNe discovered by the Palomar Transient Factory, an untargeted wide-field optical survey. They also re-analyzed metallicity measurements of 10 GRB-SNe in the literature in a consistent fashion, of which six (GRB 980425, XRF 020903, GRB 031203, GRB 060218, GRB 100316D, and GRB 120422A) are conventionally considered to be "low luminosity" (Z. Cano et al. 2017). They found that the Ic-BL SNe had statistically comparable metallicities to the GRB-SNe, but systematically lower metallicities than the Ic SNe. This observation is consistent with the predictions of the BHAD engine.

As we have shown in Section 5.1, the amount of ^{56}Ni produced in our disk models depends upon the disk properties. In the tight-binary progenitor, the angular momentum in the disk increases with the BH spin. For our current engines, we'd expect strong jets when the angular momentum is higher. Because the ^{56}Ni ejecta mass increases with angular momentum, by studying the ^{56}Ni ejecta GRB-SNe and correlating them with the power of the GRB, we can begin to probe the role of the accretion disk on the central engine. Among GRB-SNe, no correlation has been found between gamma-ray energy and nickel mass (P. K. Blanchard et al. 2024; G. P. Srinivasaragavan et al. 2024; although see L.-X. Li 2006), with the caveat that most GRB-SN nickel masses are derived using the peak luminosity of the optical light curve (Z. Cano et al. 2017). GRB 221009A (E. Burns et al. 2023; M. A. Williams et al. 2023) was a particularly extreme case: despite having $E_{\gamma,\rm iso} \sim 10^{55}$ erg, 7 orders of magnitude greater than GRB 980425 (Z. Cano et al. 2017), the SN was not more luminous than the SN associated with GRB 980425 (SN 1998bw), and there is no indication that it differed significantly from typical GRB-SNe (A. J. Levan et al. 2023; M. Shrestha et al. 2023; G. P. Srinivasaragavan et al. 2023; P. K. Blanchard et al. 2024). Is the lack of correlation due to a stochasticity in the gamma-ray emission from jets, a lack of understanding of the jet mechanism or disk nucleosynthesis, or an issue with our ^{56}Ni measurements? Observations that better constrain the mass of ^{56}Ni (e.g., late-time observations, particularly those extended to the IR, which may contribute significantly to the bolometric luminosity; J. Lyman et al. 2014) will allow us to understand the formation scenario behind tight binaries. Improved disk models to better understand disk nucleosynthesis are also important in using this observational constraint.

One of the biggest uncertainties in our tight-binary progenitor model is that we currently don't understand the method by which we eject the helium envelope. Circumstellar interactions allow us to probe the nature of the binary interactions that will shed this mass. If we see evidence of early interactions, the He-shell mass loss must have occurred after carbon ignition in the core. If we can prove that the circumstellar interactions are minor in the observed light curve, the mass loss likely occurred just after helium depletion.

In Table 3 we summarize current constraints on dense circumstellar interaction in Ic-BL SNe classified as part of ZTF's flux-limited experiment (the Bright Transient Survey;

Table 3
Signatures of Interaction in Broad-lined Ic Supernovae from ZTF's Bright Transient Survey

Description	No.
BTS Total	58
... Subset with early ∼day-cadence data	19
... ... Early fast peak (double peaked)	1
... ... Light-curve peak dominated by interaction	1
... Subset at $z \leqslant 0.04$	34
... ... Prominent late-time interaction peak	0—temp.

Note. The number of objects with clear interaction signatures in the optical light curve should be viewed as lower limits; searches for more subtle signatures will be presented in future work. Jada checking the late-time light curves.

C. Fremling et al. 2020; D. A. Perley et al. 2020). We selected the subset of events with early ∼day-cadence data (specifically, a nondetection followed by a detection the next night, and another detection 1–2 nights later): 19 events of the total of 58.[11] One of those events shows a very clear early blue peak that could be powered by interaction: SN 2020bvc (A. Y. Q. Ho et al. 2020; L. Izzo et al. 2020; J. Rho et al. 2021). Another shows an entire light curve likely dominated by interaction: SN 2018gep (A. Y. Q. Ho et al. 2019; T. A. Pritchard et al. 2021). This fraction (2/19) should be regarded as a lower limit, because other events may show more subtle signatures (e.g., not a full peak that rises then declines, but an "excess")—we will present the results of a detailed search in future work (J. L. Vail et al. 2025, in preparation). We also perform forced photometry on ZTF images (F. J. Masci et al. 2023) to search for late-time interaction signatures in the optical light curves, focusing on the objects at $z < 0.04$ (where the ZTF limiting magnitude of 20.5 mag corresponds to $M \approx -16$ mag.

Detailed observations, including broadband coverage including radio and X-ray (e.g., A. Corsi et al. 2014, 2023; M. C. Stroh et al. 2021) of these interaction events will ultimately guide us to better understanding how the broad-line Ic progenitors are formed.

8. Conclusions

In this paper, we have studied the properties of the tight-binary progenitor for GRBs under three potential engines: BHAD, NSAD, and magnetar. We compare the predicted observational features of these progenitors and engines with the observed Ic-BL SN and GRB properties. The primary results of these comparisons are as follows:

1. The preference of lGRB engines toward lower metallicity argues that the BHAD engine is the primary GRB engine under the tight-binary progenitor scenario.
2. The fact that the broader Ic-BL SNe category also exhibits this same trend suggests that the same BHAD engine drives these explosions.
3. lGRB, ultra-long GRB, LLGRB, and Ic-BL can all be explained under the tight-binary progenitor where weaker and lower Lorentz-factor outbursts are caused by binaries with the lower-mass BH formation progenitors or progenitors with wider separations.
4. Observations of shock interactions can guide our understanding of the mechanism behind mass loss that creates these tight binaries.
5. Nucleosynthetic yields from these events can provide insight into the disk properties and, in particular, the behavior of disk winds in this BHAD engine.

However, a number of additional progenitor/engine scenarios exist that have the potential to explain these observations. For example, the Induced Gravitational Collapse and its related Binary-driven Hypernova model (J. A. Rueda & R. Ruffini 2012; R. Ruffini et al. 2014), which invoke the collapse of a neutron star to a black hole also argued for a tight binary between a neutron star and a CO star. In this model, when the CO star collapses and then explodes, the accretion of its ejecta onto the neutron star causes it to collapse. To get sufficient accretion to produce a black hole, the binary must be extremely tight, which can only occur if the collapsing star is a CO, not a helium star (C. L. Fryer et al. 2014; L. Becerra et al. 2015; L. M. Becerra et al. 2024). Multidimensional models of these exploding binaries exist (L. Becerra et al. 2015; L. M. Becerra et al. 2024), but they have not been followed through light-curve calculations. As such, it is not clear whether these explosions will match the observed Ic-BL SNe.

Another progenitor is the extended mixing model that produces homogeneous stars; it tends to occur preferentially in high-mass stars (S. C. Yoon et al. 2006; L. H. Frey et al. 2013) and produce more BHAD systems with lower metallicity (S. C. Yoon et al. 2006). This progenitor paradigm also suggests that BHADs are the dominant engine. It is likely that, if strong mixing occurs, the associated supernova-like transient produced in this progenitor will tend to be Ic supernovae (with very little He and H in the ejecta). It is less clear what this progenitor predicts for the circumstellar medium or the final rotation speeds, which still dependent on the strength of coupling terms like the Spruit-Taylor dynamo.

The helium-merger model (C. L. Fryer & S. E. Woosley 1998; W. Zhang & C. L. Fryer 2001) will produce extremely rapidly spinning disks and could even explain the ultra-long GRBs (C. C. Thöne et al. 2011). It will certainly have nearby mass-ejection shells in the circumstellar medium that will affect the supernova light curves. But it is less clear how this model will not produce more type Ib over type Ic supernovae. Both the helium-merger and homogeneous star progenitors must be studied in more detail to test against the observations.

Further observations are critical to improving our understanding of the engines and progenitors of lGRBs, ultra-long GRBs, LLGRBs, and Ic-BL SNe. These include the following:

1. Improved observations of GRB durations, jet energies, and Lorentz factors as a function of environment properties (metallicity, host-galaxy characteristics) and GRB subtype. The different GRB subtypes depend on the progenitor mass and binary separation. Observations that accurately constrain the jet properties can better uncover the nature of these different explosive phenomena.
2. Trends in Ic-BL energetics comparing both GRB-SNe and normal Ic-BL to normal type Ic SNe. Trends in the energetics will provide insight into the jet mechanism and how it interacts with the collapsing star.

[11] We do not include SN 2019odp, which was subsequently reclassified as Type Ib; T. Schweyer et al. (2025).

3. Trends in the Ic-BL nucleosynthetic yields (e.g., ^{56}Ni) between different Ic classes. Peak luminosities may not be ideal constraints on the yields, and late-time or other observational methods must be developed to understand these yields. This includes helium that is either in the explosion or swept up in the explosion.
4. Evidence of or lack thereof shock interactions. This probes the timescale of mass loss, providing insight into the mechanism behind binary-interaction He mass loss. This includes broadband observations including radio and X-ray.
5. High-energy monitors built to target ultra-long and low-luminosity GRBs are key to building the observational database to test our unified picture.

These observations must be coupled with advanced theoretical understanding, including:

1. Better understanding of binary interactions to include He-star mass loss in population studies of binaries.
2. Better understanding of disk wind and jet properties.
3. Improved shock interaction studies to better take advantage of improved observations of these interactions.

Past studies of common envelope scenarios and subsequent tidal spin-up have had mixed results. R. G. Izzard et al. (2004) found that they could get the spins from tidal spin-up, but R. G. Detmers et al. (2008) argued that WR mass loss led to a rate of such systems that was too low to explain the observed GRB rate. These studies focused on hydrogen common envelope systems that leave behind helium stars. Our results concur with R. G. Detmers et al. (2008), arguing that we need some difference in the nature of stellar evolution to produce these systems. In this paper, we assume a helium common envelope phase to produce the spins necessary for angular momentum profiles to produce black hole accretion disks. As we have shown, this allows us to explain both the required angular momenta and the lack of helium in the subsequent supernova emission. R. G. Detmers et al. (2008) argued that the tight-binary interactions lead to an enhanced formation rate of compact object/helium star mergers, a.k.a., He-merger model (C. L. Fryer & S. E. Woosley 1998). This scenario does not explain the lack of observed helium in the supernova without additional assumptions (e.g., enhanced mixing).

Which solution is ultimately correct depends upon which physics prescriptions used in stellar evolution are incorrect. How we treat the evolution of stars' mass loss, stellar mixing, and the radial extent of stars remains uncertain (A. Maeder & G. Meynet 2015). For example, although standard lore argues that winds in massive stars decrease the specific angular momentum of the star, polar mass outflows can actually increase the stellar spin (A. Maeder 1999). Similarly, the composition of stars depends sensitively on the mixing (P. A. Young et al. 2005; E. Gaburov et al. 2008; L. H. Frey et al. 2013). The nucleosynthetic yields of current stellar models do not seem to match the observations of supernova remnants (C. Braun et al. 2023); improved mixing models may be required for observations beyond those of GRBs. The solution proposed in this paper is that current stellar models underestimate the expansion of the helium star, arguing that our treatment of the stellar boundary is flawed. Ultimately, understanding the progenitors of broad-line supernovae will help us pinpoint key uncertainties in stellar evolution.

With advances in observations and theory, we can both confirm/refute the tight-binary progenitor model and better understand the physics behind these powerful explosions.

Acknowledgments

The work by C.L.F. was supported by the US Department of Energy through the Los Alamos National Laboratory. Los Alamos National Laboratory is operated by Triad National Security, LLC, for the National Nuclear Security Administration of U.S. Department of Energy (contract No. 89233218CNA000001). This work was performed in part at Aspen Center for Physics, which is supported by National Science Foundation grant PHY-2210452. A.C. acknowledges support from the National Science Foundation via the grant AST-2431072, and from NASA via several Swift/GI awards.

ORCID iDs

Christopher L. Fryer https://orcid.org/0000-0003-2624-0056
Eric Burns https://orcid.org/0000-0002-2942-3379
Anna Y. Q. Ho https://orcid.org/0000-0002-9017-3567
Alessandra Corsi https://orcid.org/0000-0001-8104-3536
Amy Y. Lien https://orcid.org/0000-0002-7851-9756
Daniel A. Perley https://orcid.org/0000-0001-8472-1996
V. Ashley Villar https://orcid.org/0000-0002-5814-4061

References

Abbott, B. P., Abbott, R., Abbott, T., et al. 2017, ApJL, 848, L13
Afsariardchi, N., Drout, M. R., Khatami, D. K., et al. 2021, ApJ, 918, 89
Bambi, C., & Barausse, E. 2011, PhRvD, 84, 084034
Barnes, J., Duffell, P. C., Liu, Y., et al. 2018, ApJ, 860, 38
Becerra, L., Cipolletta, F., Fryer, C. L., Rueda, J. A., & Ruffini, R. 2015, ApJ, 812, 100
Becerra, L. M., Fryer, C. L., Rueda, J. A., & Ruffini, R. 2024, arXiv:2401.15702
Belczynski, K., Klencki, J., Fields, C. E., et al. 2020, A&A, 636, A104
Bildsten, L., & Ushomirsky, G. 2000, ApJL, 529, L33
Blanchard, P. K., Villar, V. A., Chornock, R., et al. 2024, NatAs, 8, 774
Blandford, R. D., & Znajek, R. L. 1977, MNRAS, 179, 433
Blondin, J. M., & Mezzacappa, A. 2007, Natur, 445, 58
Bloom, J. S., Djorgovski, S. G., Kulkarni, S. R., & Frail, D. A. 1998, ApJL, 507, L25
Braun, C., Safi-Harb, S., Fryer, C. L., & Zhou, P. 2023, MNRAS, 525, 6257
Burns, E., Svinkin, D., Fenimore, E., et al. 2023, ApJL, 946, L31
Burrows, A., Wang, T., Vartanyan, D., & Coleman, M. S. B. 2024, ApJ, 963, 63
Campana, S., Lodato, G., D'Avanzo, P., et al. 2011, Natur, 480, 69
Campana, S., Mangano, V., Blustin, A., et al. 2006, Natur, 442, 1008
Cano, Z., Wang, S.-Q., Dai, Z.-G., & Wu, X.-F. 2017, AdAst, 2017, 8929054
Chevalier, R. A., & Li, Z.-Y. 2000, ApJ, 536, 195
Chon, S., Omukai, K., & Schneider, R. 2021, MNRAS, 508, 4175
Colgate, S. A. 1968, CaJPh, 46, S476
Corsi, A., Ho, A. Y. Q., Cenko, S. B., et al. 2023, ApJ, 953, 179
Corsi, A., Ofek, E. O., Gal-Yam, A., et al. 2014, ApJ, 782, 42
Cucchiara, A., Veres, P., Corsi, A., et al. 2015, ApJ, 812, 122
Detmers, R. G., Langer, N., Podsiadlowski, P., & Izzard, R. G. 2008, A&A, 484, 831
Duffell, P. C., & MacFadyen, A. I. 2015, ApJ, 806, 205
Eggenberger, P., Meynet, G., Maeder, A., et al. 2008, Ap&SS, 316, 43
Eggenberger, P., Moyano, F. D., & den Hartogh, J. W. 2022, A&A, 664, L16
Faucher-Giguère, C. A., & Kaspi, V. M. 2006, ApJ, 643, 332
Frail, D. A., Kulkarni, S. R., Nicastro, L., Feroci, M., & Taylor, G. B. 1997, Natur, 389, 261
Frederiks, D., Lysenko, A., Ridnaya, A., et al. 2022, GCN, 32295, 1
Fremling, C., Miller, A. A., Sharma, Y., et al. 2020, ApJ, 895, 32
Frey, L. H., Even, W., Whalen, D. J., et al. 2013, ApJS, 204, 16
Fruchter, A. S., Levan, A. J., Strolger, L., et al. 2006, Natur, 441, 463
Fryer, C. L., Belczynski, K., Wiktorowicz, G., et al. 2012, ApJ, 749, 91
Fryer, C. L., Burns, E., Hungerford, A., et al. 2023, ApJ, 956, 19
Fryer, C. L., Fontes, C. J., Warsa, J. S., et al. 2020, ApJ, 898, 123

Fryer, C. L., & Fryer, D. A. 2025, IJMPD,
Fryer, C. L., & Heger, A. 2005, ApJ, 623, 302
Fryer, C. L., & Kalogera, V. 2001, ApJ, 554, 548
Fryer, C. L., Lien, A. Y., Fruchter, A., et al. 2022, ApJ, 929, 111
Fryer, C. L., Lloyd-Ronning, N., Wollaeger, R., et al. 2019, EPJA, 55, 132
Fryer, C. L., Mazzali, P. A., Prochaska, J., et al. 2007, PASP, 119, 1211
Fryer, C. L., & New, K. C. B. 2011, LRR, 14, 1
Fryer, C. L., Rueda, J. A., & Ruffini, R. 2014, ApJL, 793, L36
Fryer, C. L., & Woosley, S. E. 1998, ApJL, 502, L9
Fryer, C. L., Woosley, S. E., & Hartmann, D. H. 1999, ApJ, 526, 152
Fryer, C. L., & Young, P. A. 2007, ApJ, 659, 1438
Fuller, J., Piro, A. L., & Jermyn, A. S. 2019, MNRAS, 485, 3661
Gaburov, E., Lombardi, J. C., & Portegies Zwart, S. 2008, MNRAS, 383, L5
Gendre, B., Stratta, G., Atteia, J., et al. 2013, ApJ, 766, 30
Gilkis, A., Laplace, E., Arcavi, I., Shenar, T., & Schneider, F. 2025, MNRAS, Advance Access
Golenetskii, S., Aptekar, R., Frederiks, D., et al. 2013, GCN, 15260, 1
Golenetskii, S., Aptekar, R., Frederiks, D., et al. 2014, GCN, 17108, 1
Golenetskii, S., Aptekar, R., Mazets, E., et al. 2011, GCN, 12663, 1
Gompertz, B., & Fruchter, A. 2017, ApJ, 839, 49
Gottlieb, O., Jacquemin-Ide, J., Lowell, B., Tchekhovskoy, A., & Ramirez-Ruiz, E. 2023, ApJL, 952, L32
Graham, J. F., Schady, P., & Fruchter, A. S. 2023, ApJ, 954, 13
Gruber, D., Krühler, T., Foley, S., et al. 2011, A&A, 528, A15
Heger, A., Fryer, C. L., Woosley, S. E., Langer, N., & Hartmann, D. H. 2003, ApJ, 591, 288
Heger, A., Woosley, S. E., & Spruit, H. C. 2005, ApJ, 626, 350
Ho, A. Y. Q., Goldstein, D. A., Schulze, S., et al. 2019, ApJ, 887, 169
Ho, A. Y. Q., Kulkarni, S. R., Perley, D. A., et al. 2020, ApJ, 902, 86
Ho, W. C. G., & Lai, D. 2000, ApJ, 543, 386
Holland, S. T., Sbarufatti, B., Shen, R., et al. 2010, ApJ, 717, 223
Ioka, K., Hotokezaka, K., & Piran, T. 2016, ApJ, 833, 110
Ivanova, N., & Podsiadlowski, P. 2003, in From Twilight to Highlight: The Physics of Supernovae, ed. W. Hillebrandt & B. Leibundgut (Berlin: Springer-Verlag), 19
Iwamoto, K., Mazzali, P. A., Nomoto, K., et al. 1998, Natur, 395, 672
Izzard, R. G., Ramirez-Ruiz, E., & Tout, C. A. 2004, MNRAS, 348, 1215
Izzo, L., Auchettl, K., Hjorth, J., et al. 2020, A&A, 639, L11
Kaltenborn, M. A. R., Fryer, C. L., Wollaeger, R. T., et al. 2023, ApJ, 956, 71
Kann, D., Schady, P., Klose, S., et al. 2019, A&A, 624, A143
Klebesadel, R. W., Strong, I. B., & Olson, R. A. 1973, ApJL, 182, L85
Kumar, P., & Zhang, B. 2015, PhR, 561, 1
Lai, D., Chernoff, D. F., & Cordes, J. M. 2001, ApJ, 549, 1111
Lazzati, D., Morsony, B. J., Blackwell, C. H., & Begelman, M. C. 2012, ApJ, 750, 68
Lenart, A. Ł., Dainotti, M. G., Khatiya, N., et al. 2025, JHEAp, 47, 100384
Levan, A. J., Gompertz, B. P., Salafia, O. S., et al. 2024, Natur, 626, 737
Levan, A. J., Lamb, G. P., Schneider, B., et al. 2023, ApJL, 946, L28
Levan, A. J., Tanvir, N. R., Starling, R., et al. 2013, ApJ, 781, 13
Li, L.-X. 2006, MNRAS, 372, 1357
Lien, A., Sakamoto, T., Barthelmy, S. D., et al. 2016, ApJ, 829, 7
Lien, A., Sakamoto, T., Gehrels, N., et al. 2014, ApJ, 783, 24
Lloyd-Ronning, N. M., Dolence, J. C., & Fryer, C. L. 2016, MNRAS, 461, 1045
Lyman, J., Bersier, D., & James, P. 2014, MNRAS, 437, 3848
MacFadyen, A. I., & Woosley, S. E. 1999, ApJ, 524, 262
Maeder, A. 1999, A&A, 347, 185
Maeder, A., & Meynet, G. 2015, in IAU Symp. 307, New Windows on Massive Stars, ed. G. Meynet et al. (Cambridge: Cambridge Univ. Press), 9
Maistrello, M., Maccary, R., Guidorzi, C., & Amati, L. 2024, A&A, 684, L10
Margutti, R., Soderberg, A., Wieringa, M., et al. 2013, ApJ, 778, 18
Masci, F. J., Laher, R. R., Rusholme, B., et al. 2023, arXiv:2305.16279
Mazzali, P. A., Deng, J., Maeda, K., et al. 2002, ApJL, 572, L61
Meegan, C., Lichti, G., Bhat, P., et al. 2009, ApJ, 702, 791
Metzger, M. R., Djorgovski, S. G., Kulkarni, S. R., et al. 1997, Natur, 387, 878
Michel, F. C. 1985, ApJ, 290, 721
Miller, J. M., Ryan, B. R., Dolence, J. C., et al. 2019, PhRvD, 100, 023008
Miller, J. M., Sprouse, T. M., Fryer, C. L., et al. 2020, ApJ, 902, 66
Modjaz, M., Bianco, F. B., Siwek, M., et al. 2020, ApJ, 892, 153
Modjaz, M., Kewley, L., Kirshner, R. P., et al. 2008, AJ, 135, 1136
Modjaz, M., Liu, Y. Q., Bianco, F. B., & Graur, O. 2016, ApJ, 832, 108
Nakar, E., et al. 2012, ApJ, 747, 88
Nakauchi, D., Kashiyama, K., Suwa, Y., & Nakamura, T. 2013, ApJ, 778, 67
Nomoto, K., Mazzali, P. A., Nakamura, T., et al. 2001, in Supernovae and Gamma-Ray Bursts: the Greatest Explosions Since the Big Bang, ed. M. Livio, N. Panagia, & K. Sahu, 13 (Cambridge: Cambridge Univ. Press), 144
Nomoto, K., Tominaga, N., Tanaka, M., & Maeda, K. 2007, in AIP Conf. Ser. 924, The Multicolored Landscape of Compact Objects and Their Explosive Origins, ed. T. di Salvo et al. (Melville, NY: AIP), 108
Noutsos, A., Schnitzeler, D. H. F. M., Keane, E. F., Kramer, M., & Johnston, S. 2013, MNRAS, 430, 2281
Palmer, D. M., Barthelmy, S. D., Cummings, J. R., et al. 2017, GCN, 21347, 1
Panaitescu, A. 2005, MNRAS, 363, 1409
Paxton, B., Cantiello, M., Arras, P., et al. 2013, ApJS, 208, 4
Perley, D. A., Fremling, C., Sollerman, J., et al. 2020, ApJ, 904, 35
Podsiadlowski, P., Ivanova, N., Justham, S., & Rappaport, S. 2010, MNRAS, 406, 840
Popham, R., Woosley, S. E., & Fryer, C. 1999, ApJ, 518, 356
Portegies Zwart, S. F., Dewi, J., & Maccarone, T. 2005, Ap&SS, 300, 247
Pritchard, T. A., Bensch, K., Modjaz, M., et al. 2021, ApJ, 915, 121
Rantsiou, E., Burrows, A., Nordhaus, J., & Almgren, A. 2011, ApJ, 732, 57
Rastinejad, J. C., Gompertz, B. P., Levan, A. J., et al. 2022, Natur, 612, 223
Reitze, D., Adhikari, R. X., Ballmer, S., et al. 2019, BAAS, 51, 35
Rho, J., Evans, A., Geballe, T. R., et al. 2021, ApJ, 908, 232
Rodríguez, Ó., Nakar, E., & Maoz, D. 2024, Natur, 628, 733
Rueda, J. A., & Ruffini, R. 2012, ApJL, 758, L7
Ruffini, R., Muccino, M., Bianco, C. L., et al. 2014, A&A, 565, L10
Schady, P., Krühler, T., Greiner, J., et al. 2015, A&A, 579, A126
Schweyer, T., Sollerman, J., Jerkstrand, A., et al. 2025, A&A, 693, A13
Shapiro, S. L., & Teukolsky, S. A. 1983, Black Holes, White Dwarfs and Neutron Stars. The Physics of Compact Objects (New York: Wiley),
Shrestha, M., Sand, D. J., Alexander, K. D., et al. 2023, ApJL, 946, L25
Sobacchi, E., Granot, J., Bromberg, O., & Sormani, M. C. 2017, MNRAS, 472, 616
Sollerman, J., Yang, S., Perley, D., et al. 2022, A&A, 657, A64
Spruit, H. C. 2002, A&A, 381, 923
Srinivasaragavan, G. P., O'Connor, B., Cenko, S. B., et al. 2023, ApJL, 949, L39
Srinivasaragavan, G. P., Swain, V., O'Connor, B., et al. 2024, ApJL, 960, L18
Stroh, M. C., Terreran, G., Coppejans, D. L., et al. 2021, ApJL, 923, L24
Surman, R., McLaughlin, G. C., & Hix, W. R. 2006, ApJ, 643, 1057
Svensson, K. M., Levan, A. J., Tanvir, N. R., Fruchter, A. S., & Strolger, L. G. 2010, MNRAS, 405, 57
Tan, J. C., Matzner, C. D., & McKee, C. F. 2001, ApJ, 551, 946
Thöne, C. C., de Ugarte Postigo, A., Fryer, C. L., et al. 2011, Natur, 480, 72
van den Heuvel, E. P. J., & Yoon, S. C. 2007, Ap&SS, 311, 177
van Eerten, H. J. 2014, MNRAS, 445, 2414
van Putten, M. H. P. M. 1999, Sci, 284, 115
Virgili, F., Mundell, C., Pal'Shin, V., et al. 2013, ApJ, 778, 54
Wang, L. J., Wang, X. F., Cano, Z., et al. 2019, MNRAS, 489, 1110
Wheeler, J. C., Yi, I., Höflich, P., & Wang, L. 2000, ApJ, 537, 810
Williams, M. A., Kennea, J. A., Dichiara, S., et al. 2023, ApJL, 946, L24
Wongwathanarat, A., Janka, H. T., & Müller, E. 2013, A&A, 552, A126
Woosley, S., & Bloom, J. 2006, ARA&A, 44, 507
Woosley, S. E. 1993, ApJ, 405, 273
Woosley, S. E., Heger, A., & Weaver, T. A. 2002, RvMP, 74, 1015
Worley, A., Krastev, P. G., & Li, B.-A. 2008, ApJ, 685, 390
Yoon, S. C., & Langer, N. 2005, A&A, 443, 643
Yoon, S. C., Langer, N., & Norman, C. 2006, NCimB, 121, 1631
Young, P. A., Meakin, C., Arnett, D., & Fryer, C. L. 2005, ApJL, 629, L101
Zhang, B. 2018, The Physics of Gamma-ray Bursts (Cambridge: Cambridge Univ. Press),
Zhang, B., & Mészáros, P. 2001, ApJL, 552, L35
Zhang, B., & Yan, H. 2011, ApJ, 726, 90
Zhang, W., & Fryer, C. L. 2001, ApJ, 550, 357